

Tribological Properties of Surface Friction Hardened AISI 316L Steel

A. Khaksaran¹ · R. Taghiabadi¹  · M. Jafarzadegan¹

Received: 18 February 2021 / Accepted: 20 May 2021 / Published online: 31 May 2021
© The Indian Institute of Metals - IIM 2021

Abstract Friction hardening was employed to improve the tribological properties of AISI 316L austenitic stainless steel (ASS 316L). The process was conducted using a hard indenter (74 ± 1 HRC) under the travel speeds of 90, 180, and 360 mm/s for 30 and 60 passes. The results showed that FH increased the surface hardness of annealed ASS 316L alloy by 180%. The sliding wear tests also showed the positive impact of FH on the wear resistance and friction behaviour. For instance, at the applied pressure of 1 MPa, the wear rate and coefficient of friction (COF) of FHed ASS 316L sample (90 mm/s, 30 passes) were reduced by 68 and 20%, respectively, as compared to those of the annealed sample.

Keywords AISI 316L · Friction hardening · Hardness · Tribology · Friction · wear

1 Introduction

Due to their outstanding corrosion and oxidation resistance, excellent formability, non-magnetic properties, good biocompatibility, and appropriate weldability, ASSs are widely used in different field of industries [1, 2]. However, the low hardness, low yield strength, and poor tribological properties, which lead to low sliding wear resistance, high COF, and high tendency to adhesive wear [1, 3], restrict their application in the areas where high tribological properties are required.

Many attempts have been made to enhance the tribological properties of ASSs, the most important of which are thermochemical diffusion techniques such as carburizing, nitriding, and carbonitriding [4–6], electroplating [7], surface implanting [8], surface alloying [9], laser surface remelting [10], physical vapour deposition [10], surface coating [11, 12], and severe plastic deformation (SPD) techniques [10, 13, 14]. Despite high effectiveness in surface hardness improvement, they are often cost-intensive, require special equipment/materials, or can be applied on the samples with specific geometry/dimensions.

Friction hardening is a simple, cost-effective hardening method which does not significantly increase the surface temperature, does not need special equipment, and can be simply applied on flat or curved surfaces. In this process, a hard/rigid indenter is forced on the surface under a specified load and then slid in a specific direction for a definite number of passes. During this process, the surface material experiences substantial friction-induced strains producing ultrafine structures with outstanding mechanical properties [15, 16].

The impact of FH on improving the hardness/mechanical properties of Cu [17], Ta [18], carbon/constructural steels [19, 20], and metastable austenitic Cr–Ni steels [21] has been investigated. Makarov et al. [22] also showed that FH-induced surface nanostructuring increases the abrasive/adhesive wear resistance of quenched medium-carbon steels. They also showed that FH can considerably enhance the wear resistance of laser-hardened U8 (0.83 wt% C) steel [23] and reduce the COFs upon sliding friction at high speeds (more than 2.5 m/s). Shahriari et al. [24] demonstrated that FH substantially improves the dry sliding wear resistance and lowers the average COF of the Ti-6Al-4 V alloy when it is worn against a hardened steel counterface. Despite its proven effectiveness, no study has attempted so

✉ R. Taghiabadi
taghiabadi@ikiu.ac.ir

¹ Department of Materials Science, Imam Khomeini International University, Qazvin, Iran

far to improve the tribological properties of ASSs through FH treatment. On this basis, this study was conducted to investigate the effect of FH process on the surface hardness, dry sliding wear resistance, and friction behaviour of ASS 316L.

2 Materials and Methods

The FH process was performed at 25 °C using a CNC milling machine through reciprocating sliding of a hard tungsten carbide pin (74 ± 1 HRC) with the nominal diameter of 4.5 mm on the surface of annealed ASS 316L plates (16.5Cr-11.5Ni-2.4Mo-1.2Mn-0.8Si-0.03C) (in wt. %). A schematic view illustrating the FH process is shown in Fig. 1a. Figure 1b represents the geometry and dimensions of the pin and Fig. 1c shows the surface morphology of unprocessed/FH-processed regions in an FHed sample. The sliding operation was conducted at traverse speeds of 90, 180, and 360 mm/s for 30 and 60 passes. The processed samples were named according to their process parameters as a two-part number code. The first part refers to the pin traverse speed (in mm/s) and the second part (after the dash) refers to the number of passes.

The Vickers microhardness test (ASTM E384-99) was conducted at the applied load of 0.2 kg for a dwelling time of 15 s on the cross section of FHed samples from the processed surface towards their bulk. The average of six indentations is reported as the final microhardness value. The pin-on-disc dry sliding wear tests were conducted at ambient temperature and the sliding speeds of 0.1 and 0.2 m/s for a sliding distance of 1000 m under the applied pressures of 0.25, 0.5, and 1 MPa. Rectangular pins

($5 \times 5 \times 15$ mm) with a flat surface in the contact region were wire cut from the samples (Fig. 2c). A hardened AISI 52,100 steel (60 ± 2 HRC) was used as the counterface. The X-ray diffraction analysis (XRD) was conducted using a Cu-K α radiation diffractometer with a step size of 0.04 and a step time of 2 s.

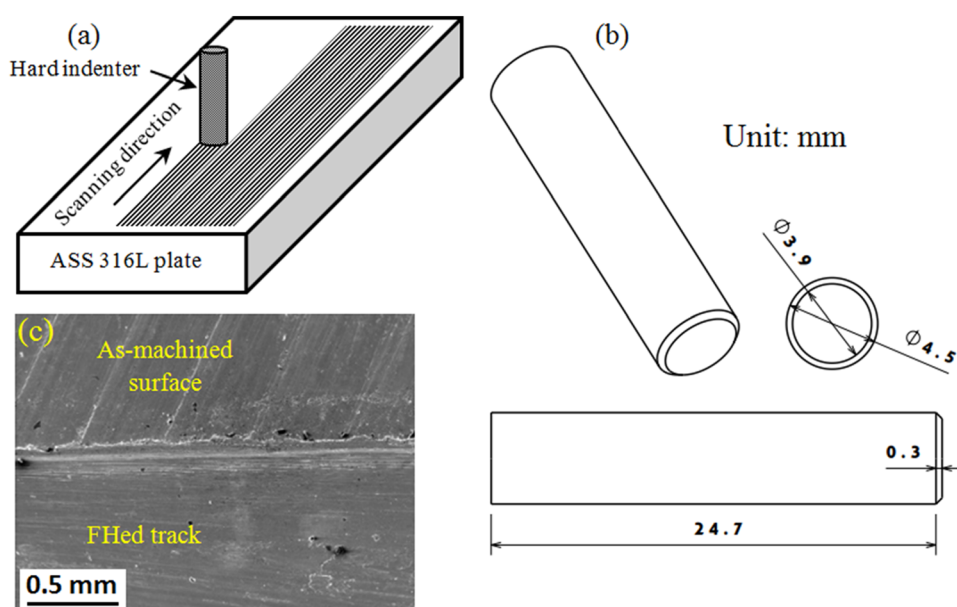
Standard metallographic procedures were carried out on metallography samples before being etched. The electrochemical etching was conducted by placing the samples as anode, an AISI 316L steel as cathode, and HNO $_3$ solution (60%) as electrolyte. The electric potential was 1 V and the current density was 0.1 A/mm 2 . An optical microscope was used for evaluating the alloys microstructure. The worn surfaces, subsurfaces, and wear debris were examined by a scanning electron microscope (SEM) equipped with an energy-dispersive X-ray spectroscopy (EDS) detector.

3 Results and Discussion

3.1 Microstructure and Hardness Analysis

The variation of subsurface microhardness of FHed samples with the depth below their treated surface is shown in Fig. 2a. As seen, the microhardness substantially increases while travelling from undeformed matrix towards the friction-treated surface. Irrespective of the processing parameters, the maximum hardness is observed at the depth of about 10–15 μ m below the FHed surface. However, the maximum hardness value is obtained at the traverse speed of 90 mm/s for the sample processed for 30 passes (Fig. 2b). Figure 2c shows the heavily deformed subsurface microstructure of 90–30 sample. As seen, the

Fig. 1 a Schematic diagram showing FH process, b the geometry and dimensions of the pin, and c the surface morphology of unprocessed/FHed regions



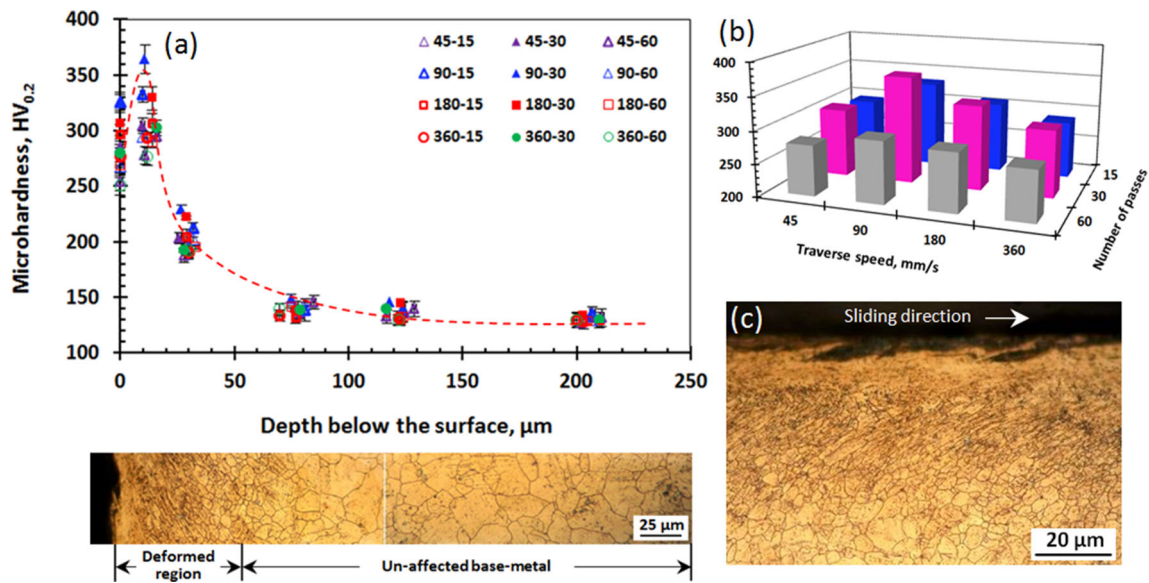


Fig. 2 **a** Microhardness profile and typical cross-sectional microstructure of the FHed samples, **b** effect of processing parameters on the maximum microhardness of FHed samples, **c** cross-sectional microstructure of 90–30 sample showing the heavily deformed surface layer

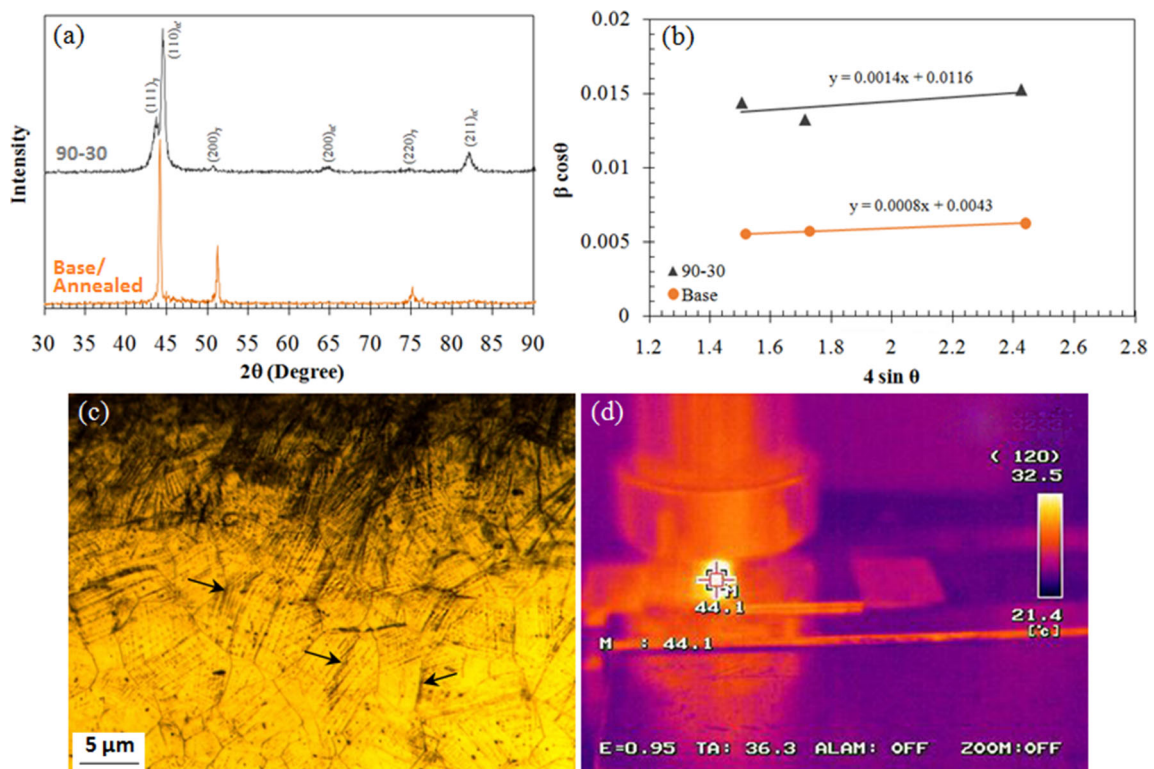


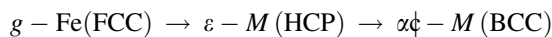
Fig. 3 **a** XRD patterns and **b** Williamson–Hall plots of the annealed and 90–30 samples, **c** formation of α'-M (shown by arrows) on the shear bands near the surface deformed layer of 90–30 sample, and **d** a typical thermographic image illustrating the maximum surface temperature of 90–30 sample during FH

unaffected (annealed) microstructure is consisted of equiaxed grains which gradually turn into the severely

deformed/refined grains while travelling towards the surface at the depth of about 50 μm below the surface.

Figure 3a compares the XRD patterns of the annealed and 90–30 samples. As seen, the new diffraction peaks appear in the XRD pattern of FHed sample which can be indexed to the formation of strain-induced α' -martensite (α' -M) [25, 26] as indicated in Fig. 3c. The formation mechanisms of strain-induced martensite in ASSs have been the focus of many studies. According to [27], applying plastic deformation produces high density of dislocations/defects and, accordingly, stacking faults as the major sources of martensitic transformation in ASSs. The stacking faults are highly ordered in the FCC lattice with hexagonal symmetry arrangement like hcp ε -martensite (ε -M) [28]. Therefore, considering the low stacking fault energy of ASS 316L [29], their emergence is likely to initiate the formation of ε -M on the close-packed (111) planes of matrix.

The ε -M plays a key role in nucleation of α' -M [26, 30]. Therefore, during the low temperature plastic deformation of ASSs (Fig. 3d), the following transformations are likely to occur, increasing the hardness/strength of the substrate with a sufficient reserve of plasticity [31]:



The above-reported phase formation sequence is in accordance with that reported in [29, 30, 32].

By using the XRD patterns, it is also possible to estimate the effect of FH on the average grain size of samples by the Williamson–Hall approach (Eq. 1) [33]:

$$\beta \cos \theta = \frac{0.9\lambda}{t} + \left(\frac{\Delta d}{d}\right) 4 \sin \theta \quad (1)$$

where λ is the wavelength of the X-ray beam, β is the line broadening at the full width at half maximum (FWHM) after subtracting the instrumental line broadening (in radians), θ is the Bragg angle (in degrees), $\left(\frac{\Delta d}{d}\right)$ is the strain, and t is the crystallite size.

If $\beta \cos \theta$ is plotted against $4 \sin \theta$, a linear trend is obtained (Fig. 3b) whose intercept value shows the crystallite size of the sample. It is evident that FH is capable of effective refining of ASS 316L grains where the average size of crystallites (as a suitable measure of the grains size) in 90–30 FHed sample is about 12 nm. The effectiveness of FH in grain refinement has been also reported elsewhere [15, 18, 34, 35]. According to these studies, upon the FH processing, lamellar dislocation cells and sub-grain boundaries are extensively formed in the affected zone. Transformation of sub-grain boundaries to the smaller substructures greatly promotes the formation of ultrafine grains in the affected region which broadens the XRD peaks.

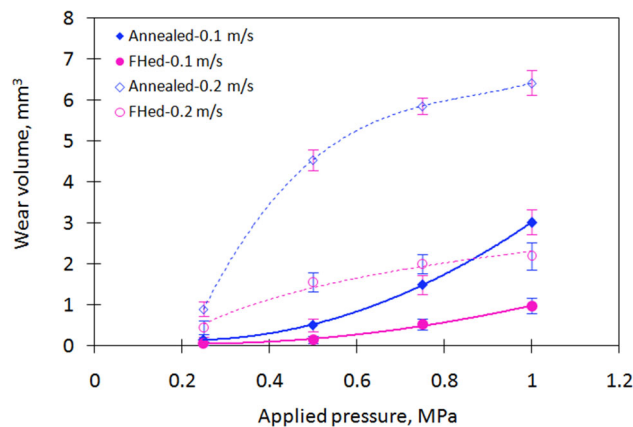


Fig. 4 Variation of wear volume of the annealed and 90–30 FHed ASS 316L samples against the applied pressure for different sliding speeds of 0.1 and 0.2 m/s

3.2 Tribological Properties

The variation of wear volume against the applied pressure at different sliding speeds of 0.1 and 0.2 m/s for the annealed and 90–30 FHed samples is shown in Fig. 4. As seen, at a given sliding speed/applied pressure, the FHed samples show lower wear as compared to the annealed sample. For instance, at the applied pressures of 0.25 and 1 MPa, the wear volume of FHed sample is lower than that of the annealed sample by 60 and 68% (for the sliding speed of 0.1 m/s) and by 50 and 65% (for the sliding speed of 0.2 m/s), respectively. It is also evident that, under the sliding speed of 0.2 m/s, the wear volume follows a decreasing trend with the applied pressure.

The volumetric wear loss of materials is adversely proportional to their hardness [36]. Therefore, as the material hardness/yield strength increases, the adhesion probability between interacting asperities decreases, leading to a lower sliding-induced substrate flow. This can improve the tribolayer stability on the worn surface. The tribolayer, which is also known as a tribo-oxide layer, is formed on the surfaces of rubbing pairs through mechano-chemical/tribo-chemical processes comprising of generation, oxidation, mechanical mixing, compaction, and tribo-sintering of wear particles [37, 38]. The tribolayer formation, depending on the type, composition, and size of its constituents as well as its bonding strength with the substrate, significantly affects the wear behaviour. This is because its existence is likely to restrict the adhesion between surfaces and, due to its low shear strength [38], it can reduce the effective COF causing less frictional heat to be generated and lower amplitude of applied surface shear strains.

Figure 5 shows the surface morphology of the annealed and 90–30 FHed samples worn at the applied pressures of 0.25 and 1 MPa under the sliding speed of 0.1 m/s.

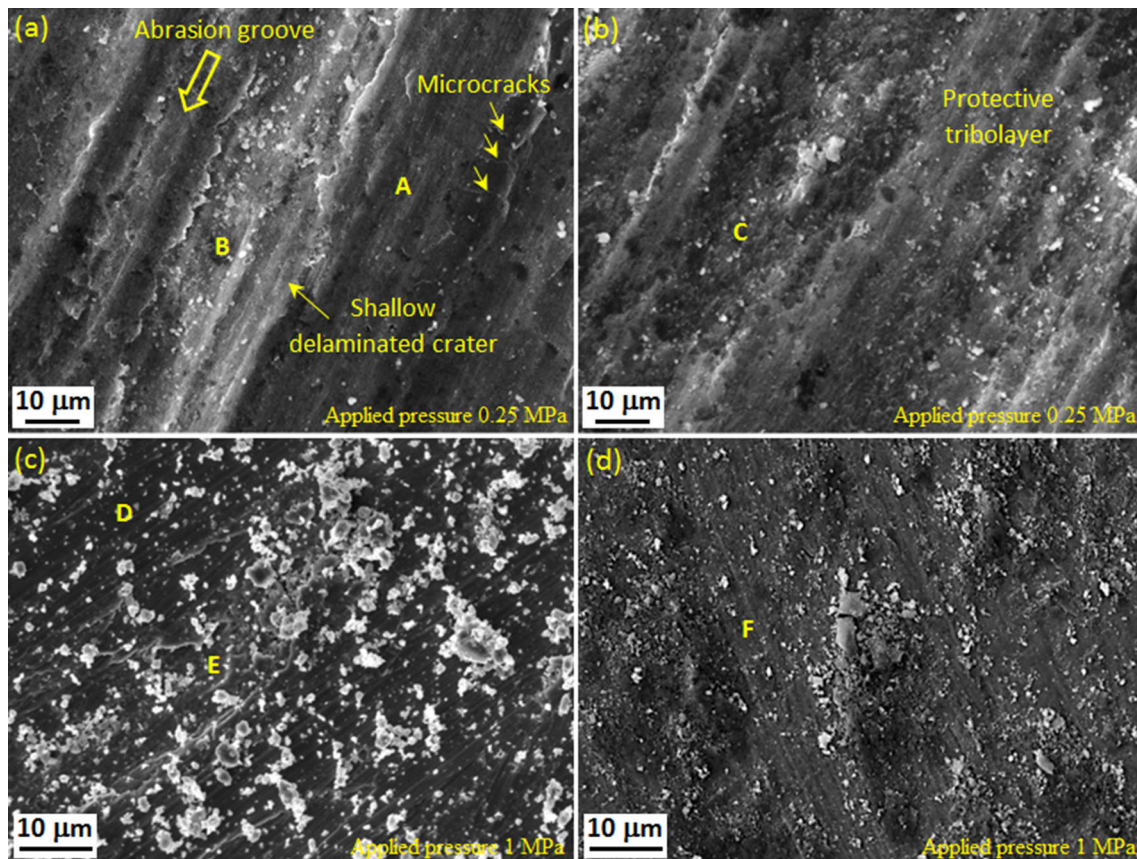


Fig. 5 Worn surface morphology of **a, c** annealed sample and **b, d** 90–30 FHed sample at the applied pressures of 0.25 and 1 MPa (sliding speed of 0.1 m/s)

Table 1 EDS analyses of the points shown in Fig. 5

	Chemical analysis, wt. %					
	O	Si	Cr	Fe	Ni	Mo
Point A	50.32	0.47	9.09	35.40	3.25	1.47
Point B	38.23	0.51	8.55	39.33	11.37	2.01
Point C	49.86	0.46	9.30	32.96	5.28	2.14
Point D	47.18	0.58	13.75	28.46	8.16	1.87
Point E	8.20	0.42	18.01	61.28	10.11	1.98
Point F	51.32	0.47	10.16	29.42	6.92	1.71

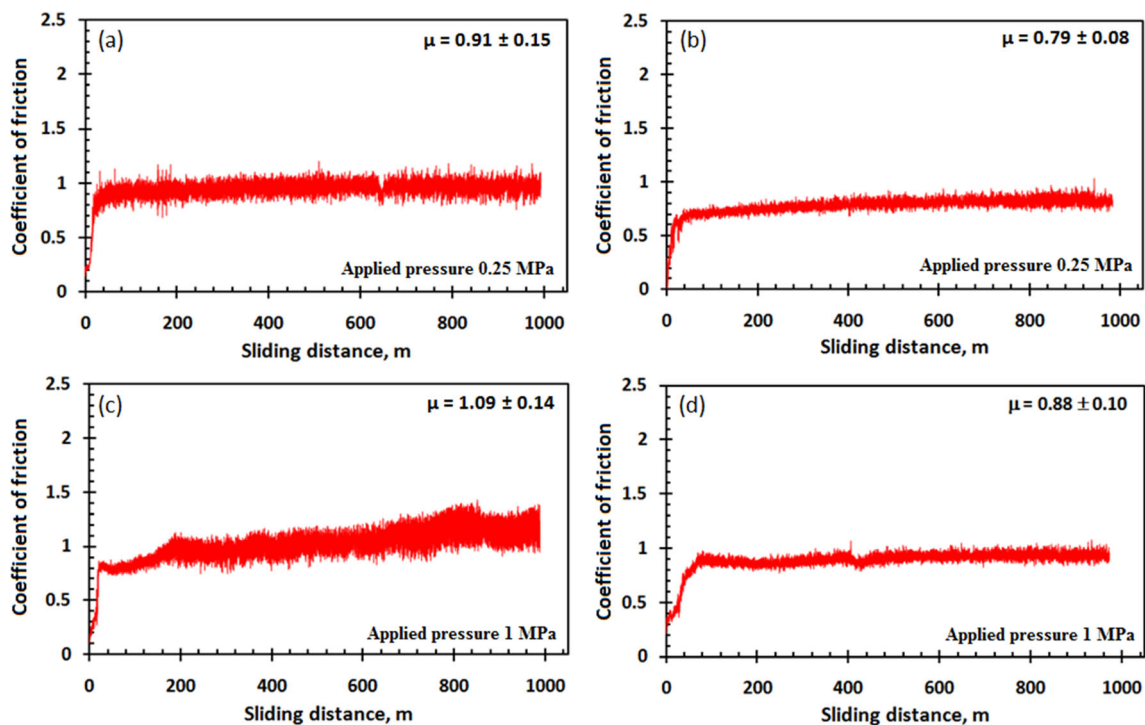
According to the EDS results (Table 1), under the applied pressure of 0.25 MPa, the worn surface of both samples has been covered by protective tribolayer. The higher amount of delaminated craters/pits and microcracks on the worn surface of the annealed sample (Fig. 5a) can be due to the lower stability of its tribolayer. However, in accordance with the wear results (Fig. 4), the low severity of surface damage, shallow depth of craters/pits, and relatively similar chemical analyses of points A and B on the worn surface of the annealed sample (Table 2) imply that,

irrespective of the applied pressure, the wear of both samples has occurred in a mild regime through oxidative wear, tribolayer delamination, and abrasion mechanisms.

Figure 6 shows the variation of COF of the annealed and 90–30 FHed samples during sliding under the applied pressures of 0.25 and 1 MPa at the sliding speed of 0.1 m/s. As seen, after an initial running-in period in which the interaction between the asperities is initiated, the steady state process is achieved where the asperities are adopted and the surfaces are in intimate contact. Higher contact

Table 2 EDS analyses of the points shown in Fig. 10

	Chemical analysis, wt. %					
	O	Si	Cr	Fe	Ni	Mo
Point A	49.19	0.53	7.14	32.94	8.32	1.88
Point B	47.94	0.50	8.49	29.25	11.92	1.90
Point C	29.36	0.56	11.47	46.91	9.88	1.82
Point D	4.48	0.47	17.34	64.58	11.06	2.07
Point E	48.17	0.51	10.40	30.19	8.81	1.92

**Fig. 6** Variation of COF against sliding distance for **a, c** annealed sample and **b, d** 90–30 FHed sample at the applied pressures of 0.25 and 1 MPa (sliding speed of 0.1 m/s)

area, surface work hardening of the sliding pairs, and activation of three-body abrasive wear have been proposed as the main factors responsible for running-in period [39]. It is evident from the COF plots that FH decreases the average value and fluctuations of COF where at the applied pressures of 0.25 and 1 MPa, the COF of FHed samples has decreased by 13% and 20%, respectively. According to the XRD analysis (Fig. 3a, b) and SEM examination of worn surfaces (Fig. 5), this can be attributed to higher substrate hardness (Fig. 2a) due to the formation of ultrafine grains and FH-induced martensite which, in turn, encourage the formation of a dense, smooth, and protective tribolayer on the worn surface of FHed sample.

The surface morphologies of the annealed and 90–30 FHed samples worn under the applied pressure of 1 MPa at

the sliding speed of 0.1 m/s are shown in Fig. 5c and d, respectively. Considering the EDS analysis results (Table 1), the surface of 90–30 FHed sample (Fig. 5d) has been covered by a protective tribolayer. However, the local detachment of tribolayer from the worn surface of the annealed sample (Fig. 5c) indicates that its wear is in a relatively severe regime.

The SEM micrographs showing the cross section of the annealed and 90–30 FHed samples worn at the applied pressure of 1 MPa are given in Fig. 7. As seen, because of the increased substrate temperature (due to the higher work of friction) and higher friction-induced shear strains, the substrate of the annealed sample experiences higher plastic deformation which, in turn, makes the tribolayer unstable and encourages its removal as wear debris. Local

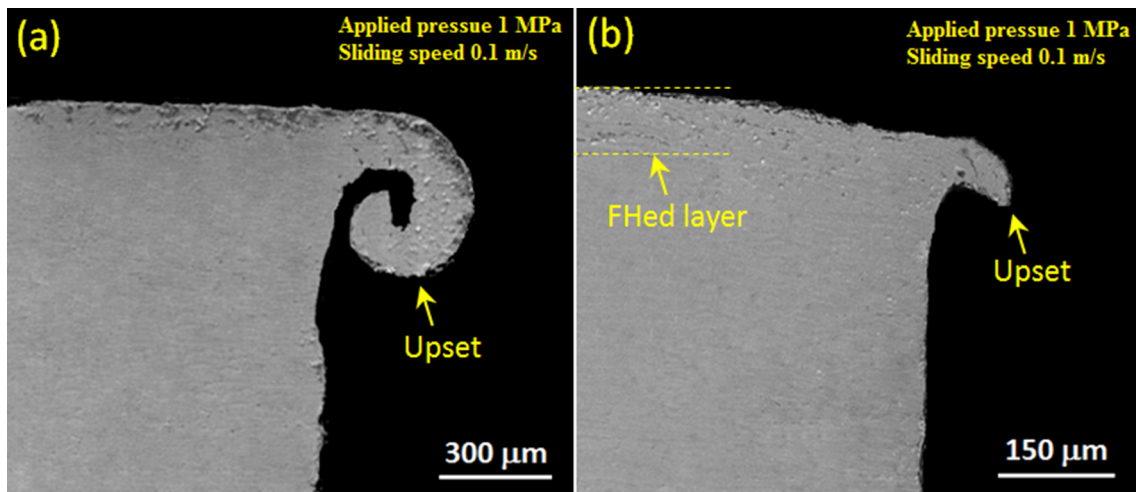


Fig. 7 Subsurface microstructure of **a** annealed and **b** 90–30 FHed samples

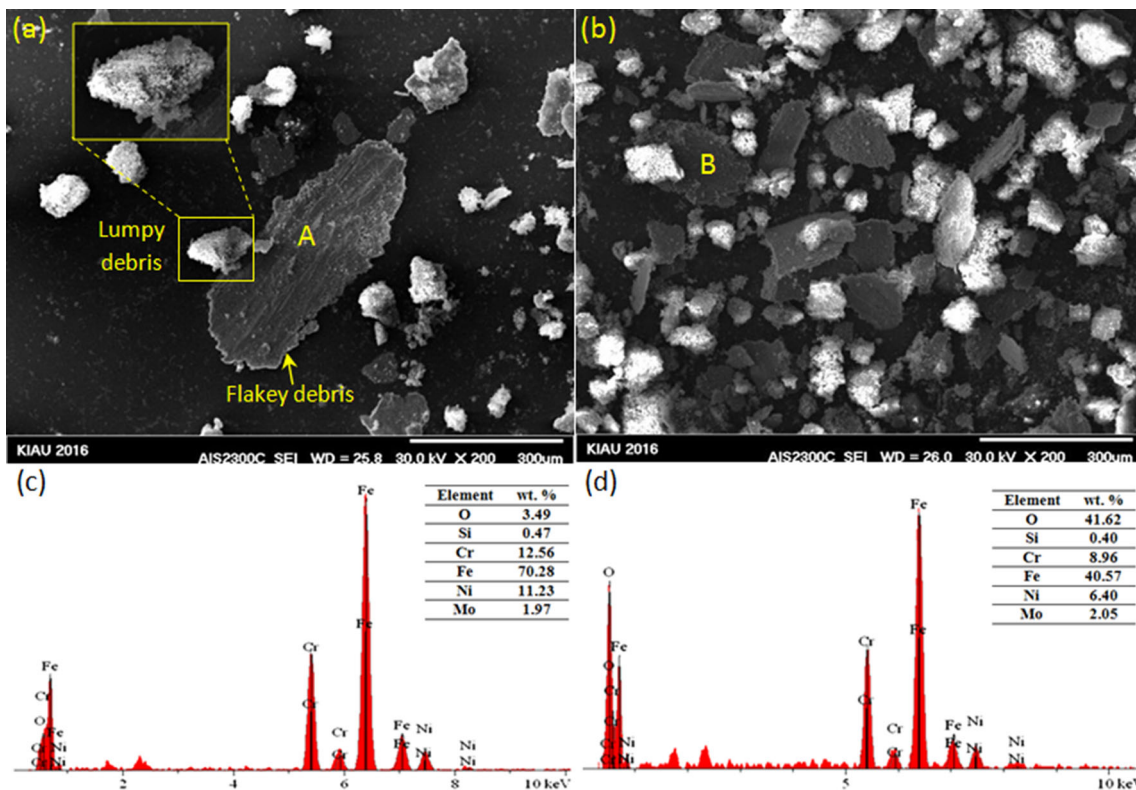


Fig. 8 **a, b** Wear debris morphology of annealed and 90–30 FHed samples, respectively, **c, d** EDS analyses of points A and B, respectively

failure of the tribolayer increases the chance of adhesion between asperities while the generation of loose debris promotes three-body abrasive wear. Therefore, as shown in Fig. 6c, an increase in the sliding speed increases the average COF and the range of its fluctuations.

The morphology and EDS analysis of the wear debris corresponding to the annealed and FHed samples worn at the applied pressure of 1 MPa and sliding distance of

0.1 m/s are shown in Fig. 8. As seen, in accordance with the surface/subsurface observations (Figs. 5 and 7), the formation of large wear particles with the analysis close to that of the metallic substrate (Fig. 8c) confirms the severe delamination of tribolayer in the annealed sample. However, the wear particles corresponding to 90–30 FHed sample include lumpy debris generated by the tribo-sintering of fine equiaxed particles and fine flaky debris. The

composition of both debris (Fig. 8d) is similar to that of the tribolayer from which they are generated (Table 1). Therefore, the oxidative wear followed by severe delamination/abrasion and localized adhesion can be regarded as the main operative mechanisms in the dry sliding wear of annealed sample. Moreover, mild delamination/abrasion of the tribo-oxide layer is believed to be the main wear mechanism in the case of 90–30 FHed sample.

The effect of the applied pressure (0.25 and 1 MPa) on the worn surface morphology of the annealed and 90–30 FHed samples after sliding at a speed of 0.2 m/s is shown in Fig. 9. Comparing these micrographs with the ones presented in Fig. 5 indicates that, irrespective of the FHed sample (Fig. 9b) whose worn surface is covered by a rather smooth and protective tribolayer with the EDS analysis shown in Table 2 (Point B), an increase in the sliding speed increases the surface damage. This is seemingly due to the thermal softening of the substrate [40–42] which decreases its potential to support the tribolayer and promotes the formation of delaminated craters, pits, and abrasion grooves (ploughs).

A fish-scale pattern, comprising of microcracks propagated normal to the sliding direction, is observed on the

tribolayer of the annealed sample worn under the applied pressure of 0.25 MPa (Fig. 9a). The tribolayer analysis is shown in Table 2 (point A). The emergence of fish-scale pattern can be attributed to the tribolayer flow through stick–slip adhesion events [43, 44]. The EDS analyses of points C and D on the worn surface of the annealed sample tested at an applied pressure of 1 MPa and sliding speed of 0.2 m/s are also shown in Table 2. In agreement with the wear results (Fig. 4), the EDS analysis of point D (Table 2) implies the severe wear of sample by local removal of its tribolayer through the plastic deformation or ploughing mechanism.

Figure 10 shows the morphology of the wear debris generated during dry sliding wear of the annealed and 90–30 FHed samples at the applied pressure of 1 MPa and the sliding speed of 0.2 m/s. The formation of relatively large metallic particles (Fig. 10a) with the EDS analysis shown in Fig. 10c implies the local complete removal of the tribolayer from the worn surface of the annealed alloy after being worn under the applied pressure of 1 MPa. At the same wear condition, the wear debris of 90–30 FHed sample (Fig. 10b) includes fine equiaxed and flake-like particles with a rather similar composition (Fig. 10d) to

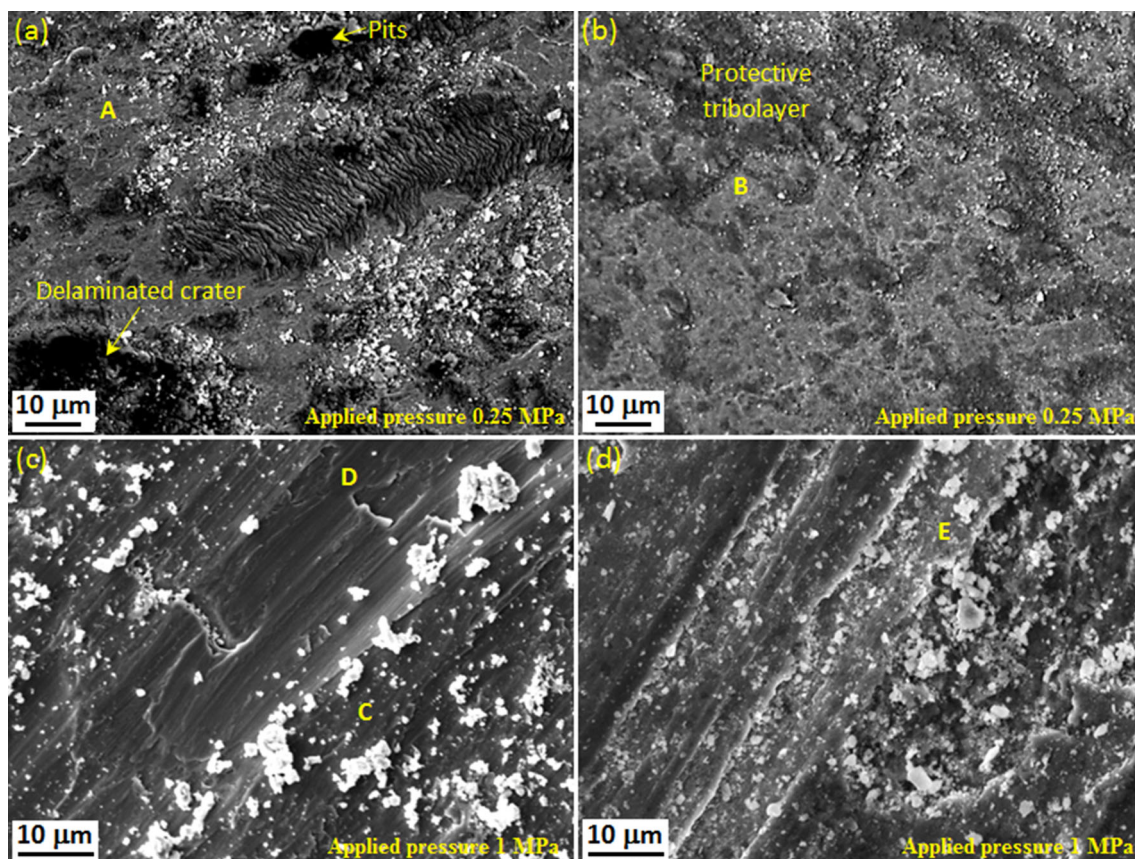


Fig. 9 Worn surface morphology of **a, c** annealed sample and **b, d** 90–30 FHed sample at the applied pressures of 0.25 and 1 MPa (sliding speed of 0.2 m/s)

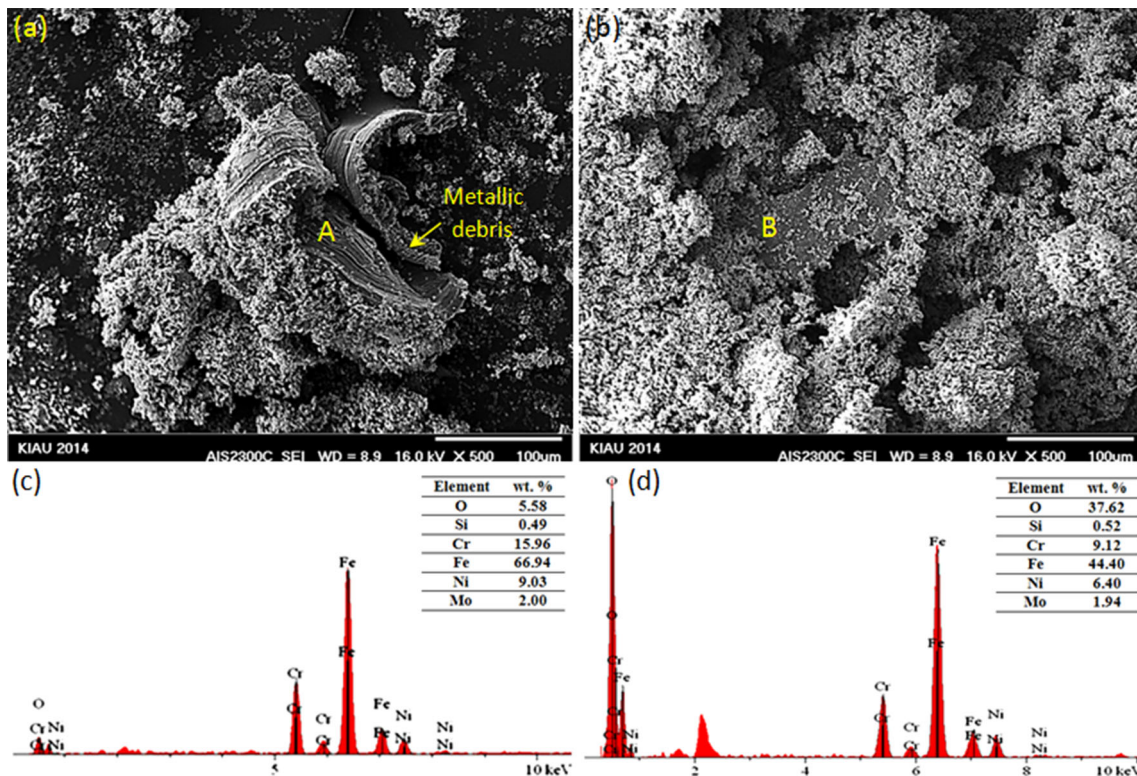


Fig. 10 a, b Wear debris morphology of annealed and 90–30 FHed samples, respectively, c, d EDS analyses of points A and B, respectively

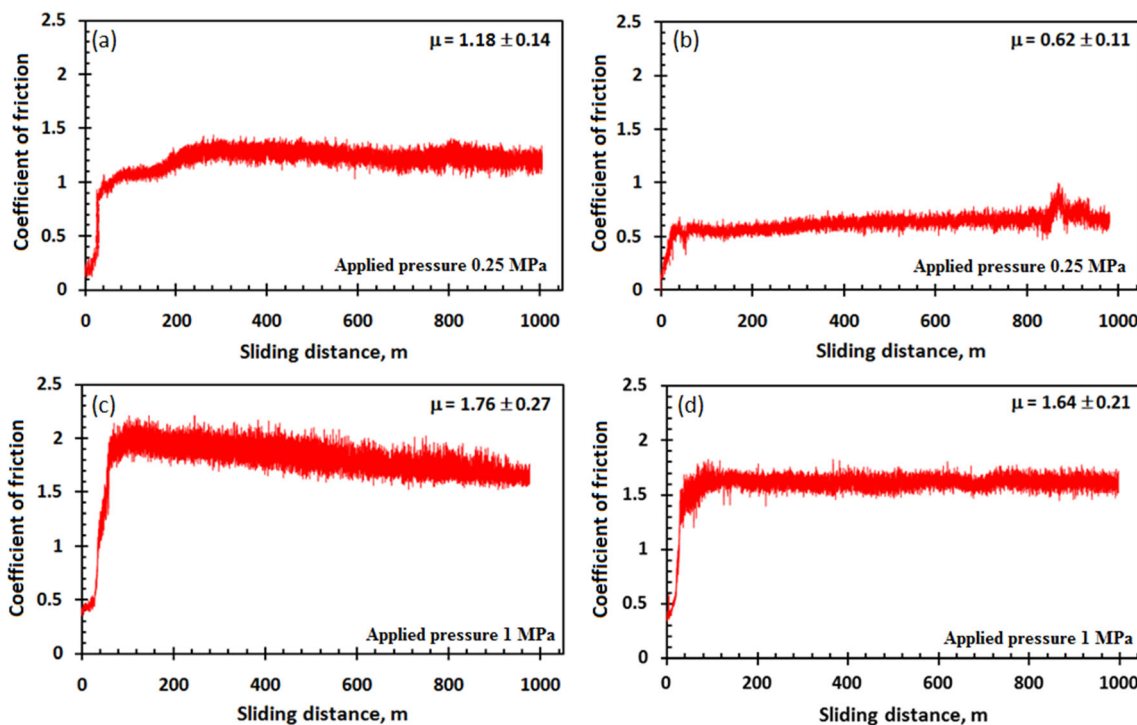


Fig. 11 Variation of COF against sliding distance for a, c annealed sample and b, d 90–30 FHed sample (sliding speed of 0.2 m/s)

that of the tribolayer from which they were generated (point E in Table 2).

Figure 11 shows the variation of COF of the annealed and 90–30 FHed samples against sliding distance under the

sliding speed of 0.2 m/s. As seen, in agreement with the worn surface/wear debris characteristics (Figs. 9 and 10), increasing the sliding speed has overall increased the average COF/COF fluctuations of the samples. However, as an exception, increasing the sliding speed under the applied pressure of 0.25 MPa has decreased the average COF of 90–30 FHed sample by about 20% (Fig. 11b) which is seemingly due to the formation of a well-compacted and smooth tribolayer on its worn surface. Though, the higher friction and friction fluctuations as the sliding speed increases can be explained by the more intense interfacial interactions, higher chance of adhesion between the contacting surfaces, friction-induced thermal softening, more delamination events, and formation of loss wear particles at higher sliding speeds.

As explained earlier, regardless of the overall increase in volumetric wear and COF, under the sliding speed of 0.2 m/s, the growth of wear volume reduces as the applied pressure increases. This probably indicates the activation of new mechanisms which counteract those promoting the wear of sample. Increased oxidation rate due to higher amounts of frictional heat generated at the higher sliding speeds especially at contacting asperities (called “flash temperature”) [45, 46] and/or the emission of exo-electrons (as potential activation energy sources promoting the tribochemical/oxidation reactions) [47, 48] as well as the friction-induced work hardening of the substrate are seemingly the main factors responsible for higher formation rate of the tribolayer than its removal rate, thereby enhancing its durability. Exo-electron emission occurs when the surface of material is excited by phenomena such as plastic deformation or abrasion and oxides or other nonmetallic surface layers need to be present in the material [47].

Considering the low stacking fault energy of austenitic stainless steels [49], the friction-induced martensite (FIM) is inevitably formed on the surface of the pin material. The higher the applied load/sliding speed in the course of sliding wear is, the higher the amount of FIM on the surface microstructure [50, 51]. The formation of martensite phase can increase the surface hardness and, accordingly, the wear resistance of ASSs provided that the process parameters are optimized. Otherwise, due to the brittle cracking of the hardened layer [52] and/or the reverse transformation or softening caused by flash temperature and accumulation of shear strain [53], the wear resistance is impaired. However, the wear results (Fig. 4) imply that the FIM formed within the range of the investigated applied loads/sliding speeds has no significant effect on the wear behaviour of the annealed samples.

4 Conclusion

- 1) FH produces a severe plastically deformed layer on the alloy surface which is characterized by ultrafine grains and formation of the stress-induced α' -martensite phase. Upon these microstructural changes, the surface hardness of the annealed sample increases by 180% in the case of the sample FHed at the sliding speed of 90 mm/s for 30 passes.
- 2) FH substantially improves the tribological properties of AISI 316L alloy. At the applied pressure of 1 MPa, the sample FHed at the sliding speed of 90 mm/s for 30 passes shows about 68% reduction in the wear rate and 20% reduction in the COF as compared to its annealed state.
- 3) The examination of worn surfaces and wear debris indicates that the wear mechanism is dominated by a combination of mild tribolayer delamination and abrasive wear for FHed alloys compared to severe delamination, adhesion, and abrasion (ploughing) in the case of the annealed samples.

Declarations

Conflict of interest The authors had no funding sources or conflict of interest to report.

References

- [1] Meng R, Deng J, Duan R, Liu Y, and Zhang G, *Opt Laser Technol* 109 (2019).
- [2] Bartolomeu F, Buciumeanu M, Pinto E, Alves N, Carvalho O, Silva F S, and Miranda G, *Addit Manuf* 16 (2017).
- [3] Bregliozzi G, Ahmed S I U, Schino A Di, Kenny J M, and Haefke H, *Tribol Lett* 17 (2004).
- [4] Barcelos M A, Barcelos MV, Filho J de S Araújo, Jr AR Franco, and Vieira E A, *REM - International Engineering Journal* 70 (2017).
- [5] Bell T, *Surf Eng* 18 (2002).
- [6] Yang S, Luo Q, Sun H, Kitchen M, and Cooke K, editors Physical and tribological properties of nitrided AISI 316 stainless steel balls. MATEC Web of Conferences; 2016.
- [7] Eriksson M, *Sliding wear performance of electroplated hard chromium and autocatalytic nickel-phosphorus coatings at elevated temperatures*, Karlstad University, (2014).
- [8] Sartowska B, Barlak M, Waliś L, Starosta W, Senatorski J, and Kosińska A, *Acta Phys Pol A* 128 (2015).
- [9] Wang H, Tang B, and Li X, *J Iron Steel Res Int* 18 (2011).
- [10] Lin N, Liu Q, Zou J, Guo J, Li D, Yuan S, Ma Y, Wang Z, and Tang B, *Materials* 9 (2016).
- [11] Owens A G, Brühl S, Simison S, Forsich C, and HeDim D, *Procedia Mater Sci* 9 (2015).
- [12] Saravanan M, Devaraju A, Venkateshwaran N, Krishnakumari A, and Saarvesh J, *Materials Today: Proceedings* 5 (2018).
- [13] Idell Y, Facco G, Kulovits A, Shankar M R, and Wiezorek J M K, *Scr Mater* 68 (2013).
- [14] El-Tahawy M, Huang Y, Um T, Choe H, Lábár J L, Langdon T G, and Gubicza J, *J Mater Res Technol* 6 (2017).

- [15] Shahriyari F, Taghiabadi R, Razaghian A, and Mahmoudi M, *J Manuf Processes* 31 (2018).
- [16] Makarov A V, Savrai R A, Pozdejeva N A, Smirnov S V, Vichuzhanin D I, Korshunov L G, and Malygina I Y, *Surf Coat Technol* 205 (2010).
- [17] Meshi L, Samuha S, Cohen SR, Laikhtman A, Moshkovich A, Perfilyev V, Lapsker I, and Rapoport L, *Acta Mater* 59 (2011).
- [18] Zhang YS, Wei QM, Niu HZ, Li YS, Chen C, Yu ZT, Bai XF, and Zhang PX, *Int J Refract Met Hard Mater* 45 (2014).
- [19] Makarov AV, Korshunov LG, Vykhodets VB, Kurennykh TE, and Savrai RA, *Physics of Metals and Metallography* 110 (2010).
- [20] Vychuzhanin DI, Makarov AV, Smirnov SV, Pozdeeva NV, and Malygina IY, *Journal of Machinery Manufacture and Reliability* 40 (2011).
- [21] Baraz VR, and Fedorenko ON, *Russ Metall* 2013 (2013).
- [22] Makarov AV, Pozdejeva NA, Savrai RA, Yurovskikh AS, and Malygina IY, *J Frict Wear* 33 (2012).
- [23] Makarov AV, Korshunov LG, Malygina IY, and Solodova IL, *Met Sci Heat Treat* 49 (2007). <https://doi.org/10.1016/j.jmapro.2017.12.016>
- [24] Shahriari F, Taghiabadi R, Razaghian A, and Mahmoudi M. *J Manufact Process*, 31 (2018).
- [25] Shen YF, Li XX, Sun X, Wang YD, and Zuo L, *Mater Sci Eng, A* 552 (2012).
- [26] Scheriau S, Zhang Z, Kleber S, and Pippan R, *Mater Sci Eng, A* 528 (2011).
- [27] Mumtaz K, Takahashi S, Echigoya J, Kamada Y, Zhang LF, Kikuchi H, Ara K, and Sato M, *J Mater Sci* 39 (2004).
- [28] Martin S, Ullrich C, and Rafaja D, *Materials Today: Proceedings* 2 (2015).
- [29] Gubicza J, El-Tahawy M, Huang Y, Choi H, Choe H, Lábár JL, and Langdon TG, *Mater Sci Eng, A* 657 (2016).
- [30] Lee TH, Ha HY, Kang JY, Moon J, Lee CH, and Park SJ, *Acta Mater* 61 (2013).
- [31] Bak S, Abro M, and Lee D, *Metals* 6 (2016).
- [32] Kireeva IV, and Chumlyakov YI, *Physics of Metals and Metallography* 101 (2006).
- [33] Zhang YS, Li WL, Wang G, Zhang LC, Yao B, and Han Z, *Mater Lett* 68 (2012).
- [34] Dai K, and Shaw L, *Mater Sci Eng, A* 463 (2007).
- [35] Zhang YS, Zhang PX, Niu HZ, Chen C, Wang G, Xiao DH, Chen XH, Yu ZT, Yuan SB, and Bai XF, *Mater Sci Eng A* 607 (2014).
- [36] Archard JF, *J Appl Phys* 24 (1953).
- [37] Lu ZC, Zeng MQ, Gao Y, and Zhu M, *Wear* 304 (2013).
- [38] Soustani M Fekri, Taghiabadi R, Jafarzadegan M, Shahriyari F, and Rahmani A, *J Tribol* 141 (2019).
- [39] Nadim A, Taghiabadi R, and Razaghian A, *J Tribol* 140 (2018).
- [40] Pouladvand S, Taghiabadi R, and Shahriyari F, *J Mater Eng Perform* 27 (2018). <https://doi.org/10.1007/s11665-018-3420-9>.
- [41] Wang Y, Zhang L, Xiao J, Chen W, Feng C, Gan X, and Zhou K, *Tribol Int* 94 (2016).
- [42] Haq MI Ul, and Anand A, *Silicon* 11 (2018).
- [43] Khanna R, and Basu B, *J Am Ceram Soc* 90 (2007).
- [44] Luo K, *Lubricants* 58(6) (2018).
- [45] Mondal MK, Biswas K, and Maity J, *Metall Mater Trans A* 47(2015).
- [46] Straffelini G, and Molinari A, *Tribol Lett*, 41(2010).
- [47] Tran BH, Tieu AK, Wan S, Zhu H, Mitchell DRG, and Nancarrow MJ, *Journal of Physical Chemistry C* 121 (2017).
- [48] Kajdas CK, *Tribol Int* 38(2005)
- [49] Mao B, Chu S, and Wang S, *Metals* 10(9) (2020).
- [50] Lee YS, Kondo Y, and Okayasu M, *Metals* 10 (2020).
- [51] Wei X, Hua M, Xue Z, and Li J, *Wear* 267 (2009).
- [52] Jost N, and Schmidt I, *Wear* 111 (1986).
- [53] Lee YS, Ishikawa K, and Okayasu M, *Met Mater Int* 25 (2018).

Publisher's Note Springer Nature remains neutral with regard to jurisdictional claims in published maps and institutional affiliations.